Journal of Rock Mechanics and Geotechnical Engineering 15 (2023) 204–215

Contents lists available at ScienceDirect

Journal of Rock Mechanics and Geotechnical Engineering

journal homepage: www.jrmge.cn

Full Length Article

Method for visualizing the shear process of rock joints using 3D laser scanning and 3D printing techniques

Man Huang [a], Chenjie Hong [a,b], Peng Sha [a,*], Shigui Du [a,c], Zhanyou Luo [c], Zhigang Tao [b]

[a] School of Civil Engineering, Shaoxing University, Shaoxing, 312000, China
[b] School of Mechanics and Civil Engineering, China University of Mining and Technology, Beijing, 100083, China
[c] School of Civil and Environmental Engineering, Ningbo University, Ningbo, 315000, China

ARTICLE INFO

Article history:
Received 7 October 2021
Received in revised form
3 January 2022
Accepted 23 February 2022
Available online 12 April 2022

Keywords:
Rock joint
Shear test
Three-dimensional printing (3DP)
Three-dimensional laser scanning (3DLS)
Visualization approach

ABSTRACT

This study presents a visualized approach for tracking joint surface morphology. Three-dimensional laser scanning (3DLS) and 3D printing (3DP) techniques are adopted to record progressive failure during rock joint shearing. The 3DP resin is used to create transparent specimens to reproduce the surface morphology of a natural joint precisely. The freezing method is employed to enhance the mechanical properties of the 3DP specimens to reproduce the properties of hard rock more accurately. A video camera containing a charge-coupled device (CCD) camera is utilized to record the evolution of damaged area of joint surface during the direct shear test. The optimal shooting distance and shooting angle are recommended to be 800 mm and 40°, respectively. The images captured by the CCD camera are corrected to quantitatively describe the damaged area on the joint surface. Verification indicates that this method can accurately describe the total sheared areas at different shear stages. These findings may contribute to elucidating the shear behavior of rock joints.

1. Introduction

Failure generally occurs along rock discontinuity, such as joint, which is a major factor governing the inhomogeneity and anisotropy of rock masses (Barton, 2013). Thus, the shearing behaviors of natural joints and other discontinuities affect the strength and deformation of rock mass. This dominates the stability of geotechnical engineering projects, such as underground excavation, rock slope construction, and resource exploitation (Barton, 1973; Kulatilake and Shou, 1995; Grasselli and Egger, 2003; Özgür et al., 2015).

Numerous experimental investigations have been performed to quantitatively characterize the mechanical properties of natural rock joints. Several external monitoring techniques, including acoustic emission, infrared thermal imaging, and charge-coupled device (CCD) camera, have proven to be appropriate for monitoring the failure of specimens in real time (Tan et al., 2007; Koyama et al., 2008; Ishida et al., 2010; Hedayat et al., 2014). The peak shear strength of rock joints significantly decreases with the degradation of the joint surface roughness after multiple shearing events (Johnston and Lam, 1989; Jing et al., 1993; Lee et al., 2001; Singh et al., 2002; Jafari et al., 2004; Li et al., 2014). Based on laboratory test results, various shear strength models have been proposed to evaluate the mechanical properties of natural rock joints (Barton, 1977; Saeb and Amadei, 1992; Grasselli et al., 2002, 2006; Ge et al., 2016; Zhang et al., 2016; Asadizadeh et al., 2017). Previous research indicates that the morphological characteristics of a rock joint have a substantial influence on its shearing mechanism. Nevertheless, the lack of joint specimens with the same joint surface morphology has always limited the experimental studies because no two natural rock joints are completely identical. Measuring the shearing process of natural rock joints directly remains a challenge in rock mechanics. The progressive failure on the surface of a specimen is easier to be detected than that within the specimen. Although computerized tomography (CT) scanning is capable of interiorly monitoring the failure of specimens in real time (Peng et al., 2018), it can only be applied to small specimens due to the high cost for detection and slow speed for imaging. Hence, inverse engineering technology is used to produce artificial rock joint models for experimental studies and numerical simulations (Roosta et al., 2006; Huang et al., 2013; Park and Song, 2013;

* Corresponding author.
E-mail address: shapeng@usx.edu.cn (P. Sha).
Peer review under responsibility of Institute of Rock and Soil Mechanics, Chinese Academy of Sciences.

https://doi.org/10.1016/j.jrmge.2022.02.013

Xia et al., 2014; Fan et al., 2019). Despite the widespread acceptance of this method, such models cannot represent natural rocks due to their irregular surface shapes (Jiang et al., 2016a). Comparatively, three-dimensional printing (3DP) method is capable of repeatedly producing artificial specimens by various materials with complex geometry of natural rocks (Fereshtenejad et al., 2016; Pua et al., 2018; Zhou et al., 2019; Jaber et al., 2020). Combined with three-dimensional laser scanning (3DLS), 3DP can be used to perform a comparative analysis of the 3D morphology of realistic rock joints before and after shearing (Tang et al., 2012; Zhang et al., 2014; Babanouri and Karimi, 2015; Jiang et al., 2016a; Kumar and Verma, 2016). In previous studies, it has been proven that the developed 3DLS and 3DP techniques provide a new way to manufacture experimental specimens of rock joints (Jiang and Zhao, 2015; Ju et al., 2017, 2018). Different rock-like materials, such as concrete and gypsum, are adopted to build 3D joint, including the upper and lower blocks. However, compared with the shear characteristics at failure, how to obtain a complete wear process of asperities during tests is still a challenge. Furthermore, the similitude of the mechanical behaviors of the printed models and natural rocks is not well understood.

Therefore, this study proposes a monitoring method to assess the evolution of surface roughness inside specimens based on a visualized shear test. The 3DLS and 3DP techniques are adopted to construct a transparent model of a rock joint. A visualized monitoring method is created with a CCD camera to observe the progressive failure during direct shearing. The combination of these methods is conducive to overcoming the limitations of existing methods and can be used to describe the evolution of rock joint's surface morphology during shearing and elucidate the shear mechanism.

2. Preparation of 3DP joint specimen

2.1. Selection of 3DP material

Two types of available 3DP materials, including (i) powder-based materials, i.e. ceramics (Chen et al., 2019), gypsum powders (Jiang et al., 2016b; Kong et al., 2018), polymethyl methacrylate (Jiang et al., 2016b), and (ii) stereo lithography apparatus (SLA)-produced materials, i.e. soluble release support materials (SR20, SR30, etc.) and resin (Liu et al., 2016; Ju et al., 2018), are utilized in the field of rock mechanics. Among these 3DP materials, the resin can be directly observed during tests due to its transparency (Liu et al., 2016). It is possible to analyze the progressive failure of resin with internal discontinuities during direct shear test. Therefore, a 3DP resin model is relatively suitable for simulating natural rocks in the present study.

We adopted a type of transparent photopolymer resin called VeroClear 810 to print the specimens. This material has been successfully employed to produce a physical model that represents natural rock (Ju et al., 2017; Kuo et al., 2017; Wang et al., 2017; Liu et al., 2020; Xia et al., 2020). The elastic modulus (E) and Poisson's ratio (ν) of VeroClear 810 differ greatly from those of natural rocks at room temperature (10 °C), as summarized in Table 1. Hence the mechanical properties of VeroClear 810 need enhancement for mimicking the natural rocks test. The mechanical behavior of resin is temperature-dependent, and the mechanical properties can significantly change with the testing temperature (Wu et al., 2005). To effectively replicate natural rocks with VeroClear 810, a freezing method can be applied to enhancing its mechanical properties (Zhou and Zhu, 2018).

Table 1
Mechanical properties of the 3DP material and natural rocks at room temperature (10 °C).

Specimen	σ_c (MPa)	σ_t (MPa)	E (GPa)	ν	Source
VeroClear 810	76.7	54.5	3.1	0.38	Ju et al. (2014)
	81.6	38.1	3.1	0.38	Wang et al. (2017)
	82.4	/	3.11	0.38	Xia et al. (2020)
	75.7	38.1	2.9	0.35	Liu et al. (2016)
	84.3	50–65	2–3	/	Kuo et al. (2017)
Carrara marble	84.6	6.9	49	0.2	Wong and Einstein (2009)
Xiaowan gneiss	98.5	7.39	42	0.18	Wu et al. (2009)
Beishan granite	97.3	10.59	53	0.22	Zhao et al. (2014)

Note: σ_c is the uniaxial compressive strength (UCS) and σ_t is the tensile strength.

2.2. Enhancement of mechanical properties

Four groups of UCS tests were performed to obtain the mechanical behavior and basic properties of the VeroClear 810 specimens under different temperatures (i.e. 10 °C, 0 °C, −30 °C and −45 °C). A universal testing machine (WAW-600, SUNS, China) with a loading capacity of 600 kN was used to load the specimens (Fig. 1). The velocity of the loading cell was set at 2 mm/min. The 3DP specimens were generated using an Object Connex 500 3D printer with dimensions of ϕ25 mm × 50 mm (Fig. 2a). Resin specimens were frozen in a cooler for at least 24 h prior to testing to maintain the mechanical properties of the 3DP resin specimens with a low-temperature treatment. A thermocouple was placed on the surface of the specimen to measure its temperature during the test. Given that some temperatures (i.e. −30 °C and −45 °C) were beyond the service temperature of the strain gage generally used in rock tests, the axial strain was recorded using loading machine sensors only.

Fig. 3 illustrates the axial stress–strain curves of the 3DP resin specimens recorded during UCS tests at laboratory temperature (10 °C) and after refrigeration (i.e. 0 °C, −30 °C and −45 °C). Given that strain gages were not employed, the lateral strain of the resin specimens was obtained from the CCD camera. In addition, the lateral strain of the resin specimen at −45 °C was not monitored because of sudden brittle failure, whereas the specimen at 10 °C deformed as a typical ductile material after the peak stress was reached. Table 2 shows the physical properties of the four specimens. The UCS (σ_c) and elastic modulus (E) of the frozen 3DP resin specimens increase by 35% at −30 °C and 76.5% at −45 °C, due to refrigeration. The Poisson's ratio (ν) decreases as the temperature decreases.

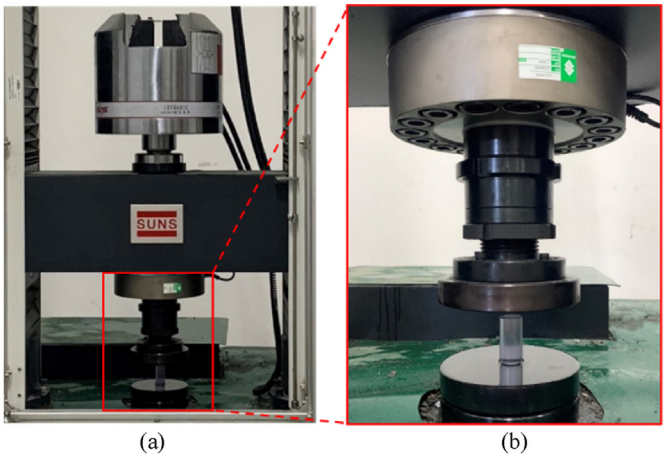

Fig. 1. UCS tests for VeroClear 810 specimens: (a) SUNS universal testing machine with a loading capacity of 600 kN and (b) UCS specimen made by VeroClear 810, which is 25 mm in diameter and 50 mm in length.

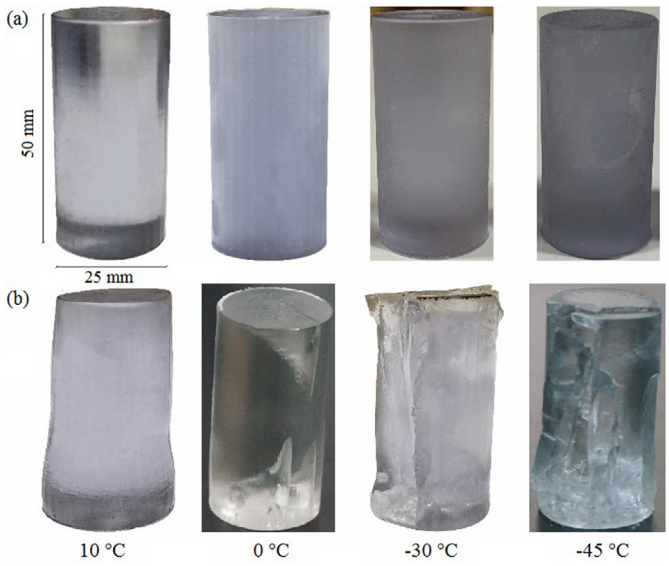

Fig. 2. The 3DP specimens (a) before and (b) after UCS tests under different temperatures.

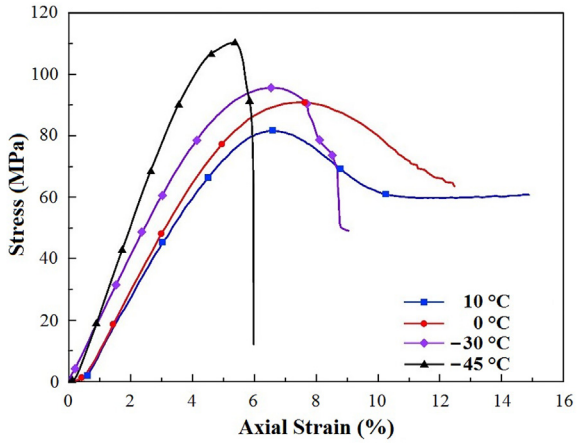

Fig. 3. Stress–strain curves of the 3DP samples at different temperatures.

Table 2
Mechanical properties of the 3DP resin samples at different temperatures.

Sample and temperature	σ_c (MPa)	E (GPa)	ν
Intact resin at 10 °C	81.6	1.7	0.38
Frozen intact resin at 0 °C	90.86	1.95	0.34
Frozen intact resin at −30 °C	95.565	2	0.33
Frozen intact resin at −45 °C	110.2	3	

Fig. 2b displays the specimens after UCS test at different temperatures. The specimen at 10 °C exhibited high ductility during the final loading stage. The failure modes of the 3DP specimens were comparable to that of brittle rocks when the pre-treatment temperature is below −30 °C. The stress-strain curve of specimen at −45 °C rapidly drops after the peak stress, as shown in Fig. 3. In addition, the frozen resin specimen exhibited spalling failure, with fragments ejecting outward. Fig. 4 shows the fragments of the 3DP specimen at −45 °C after failure. The existence of strip fragments indicated splitting failure, similar to the fragments of some natural rocks which is hard and brittle. The experimental results indicate that the low-temperature treatment can change the mechanical

Fig. 4. The broken 3DP specimen at −45 °C after UCS test.

properties of VeroClear 810, which is close to those of natural rocks. Also, the mechanical responses of the 3DP resins exhibited similarly to some brittle rocks. Therefore, if the temperature is almost constant (lower than −30 °C) during tests, the 3DP specimen can well mimic natural rocks.

2.3. Production of 3DP joint specimen

The surface of a natural joint can be digitized and reconstructed using the 3DLS and 3DP techniques, and the procedure includes three main steps.

(1) Step 1: Acquisition of digital joint surface

When a natural joint specimen was studied, a portable laser scanner (MetraSCAN 3D, Creaform, Canada) was used to obtain point clouds with a scanning accuracy of 0.02 mm (Fig. 5a). The corresponding software can reconstruct the joint surface from the

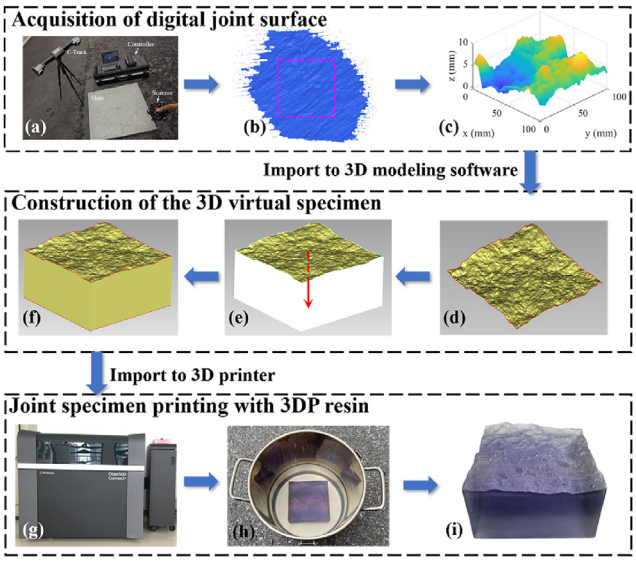

Fig. 5. Preparation of 3DP joint specimen: (a) The 3DLS facility (MetraSCAN 3D, Creaform) and working set-up; (b) Original 3D point cloud representing the rock joint; (c) The 3D digital surface reconstruction of the natural joint; (d) Stereo lithography (STL) format of 3D digital surface; (e) Projecting process of the digital surface; (f) The 3D virtual joint specimen (upper block); (g) The 3D printer adopted in this work (Objet500, Stratasys); (h) Removing process of the support material (SUP706 in this work) within a solution including 2% NaOH and 1% Na2SiO3; and (i) The 3D transparent joint specimen (upper block).

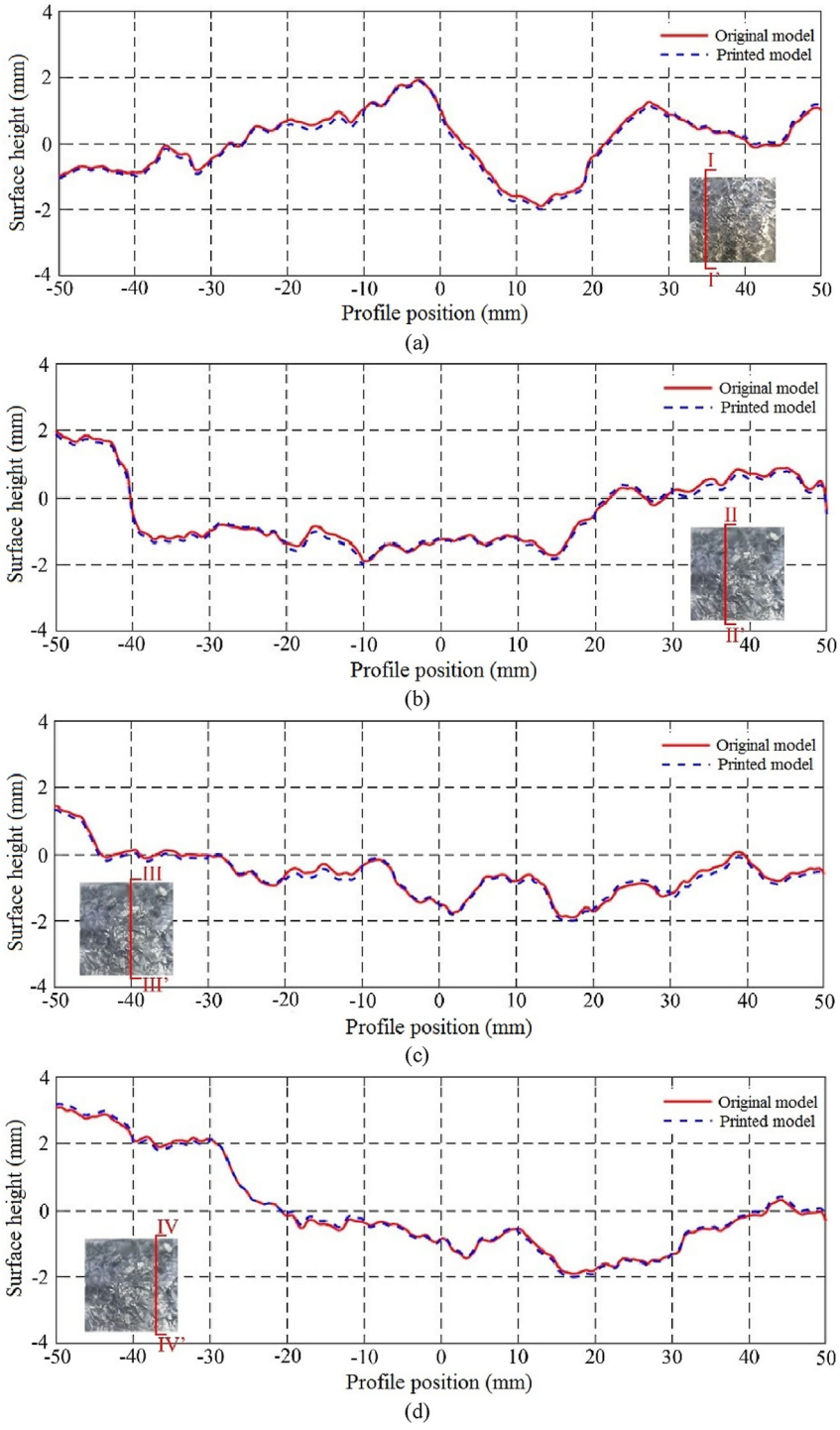

Fig. 6. Direct comparisons of the 2D profile lines between two specimens: (a) Section I-I′, (b) Section II-II′, (c) Section III-III′, and (d) Section IV-IV′.

point clouds using a triangular irregular network (TIN) mesh (Grasselli, 2001). The initial digital surface was first input into the 3D modeling software (Geomagic Studio) to remove a few points corresponding to noise. If the scanning region is larger than the size of the surface of interest, it is necessary to constrain the 3D digital surface by removing the superfluous part (Fig. 5b). According to the size of the joints in the subsequent experiment, we consider a digital joint surface with a size of 100 mm × 100 mm, as shown in Fig. 5c.

(2) Step 2: Construction of the 3D virtual specimen

The file of digital surface was converted to the stereo lithography (STL) format (Fig. 5d) that is readable by the 3D printing software. The thickness of the 3D virtual specimen should be set as 50 mm, a half of the length of the standard rock specimen, which is calculated from the center point of the digital surface. Then, the virtual joint surface was projected onto the plane based on the thickness, which was regarded as the bottom of the model (Fig. 5e).

Finally, a 3D virtual specimen (lower block) was obtained by closing the space between the digital surface and the projection plane (Fig. 5f). The upper block was obtained by projecting the same distance in the opposite direction. Once the two blocks of the 3D virtual joint specimens were generated, a 3D model can be produced using 3DP technology.

(3) Step 3: Printing the physical joint specimen with resin

Taking the lower block as an example, the STL file was first imported into the 3D printer (Objet500, Stratasys, USA, see Fig. 5g). VeroClear 810 was selected as the printing material. Since VeroClear 810 is a type of liquid polymer, a support material should be adopted to fix the model before solidification. The supporting material should be water-soluble, low-strength and physically removable or washed easily after the specimen is prepared. The gelling material SUP706 was selected as the support material in this study. The printed model was solidified by ultraviolet light during printing. Afterward, the 3DP specimen was placed in a solution (including 2% NaOH and 1% Na_2SiO_3) for 24 h (Fig. 5h). Because the solubilities of VeroClear 810 and SUP706 are different, the solution can soften the support material attached to the outside of the 3DP model. Finally, a transparent joint specimen was completed after rinsing with high-pressure water, as shown in Fig. 5i.

The final resin joint specimen was the result of 3DLS, computer-aided reconstruction, and 3DP. The differences in surface shape between the replicated and original joints exist, which should be evaluated before the shear test. Therefore, a geometrical error analysis of the 3DP joint specimen is required to perform. A direct comparison of the two-dimensional (2D) profile lines of two joint specimens was conducted using a portable laser scanner (Fig. 6). The results revealed that the errors in average height between the two joint surfaces were basically within 0.18 mm. This investigation indicates the modeling method for rock joints using 3DLS and 3DP techniques is fairly precise. Considering that damaged area occurred locally during shearing, we divided the surface of the upper block of 3DP joint specimen evenly into 25 small grids and color it with propylene red pigment so that the joint surface could be easily observed (Fig. 7).

3. Shear process visualization

3.1. Photographic equipment

The wide use of CCD camera in scientific investigations makes it possible to acquire high-spatial-resolution images and analyze them in near real time (Tohsing et al., 2013). Thus, we used a CCD camera in the laboratory (Y7−S3, IDT, USA) to track the changes in the joint surface during the shearing process, and its parameters are listed in Table 3. Before the shear test, the positional relationship between the CCD camera and 3DP joint specimen should be determined. According to the lens imaging (Fig. 8a), the object distance (OD) could be calculated as

$$OD = \frac{W_f f}{w_c} \tag{1}$$

where W_f is the width of the field of view, w_c is the width of the CCD sensor, and f is the image distance. To ensure that the entire shear process is recorded by the CCD sensor (Fig. 8b), W_f should be larger than $L + \Delta d$, where L is the length of joint specimen and Δd is the shear displacement. In this study, L is 100 mm and Δd is set to be 10% of L based on the suggested method from International Society for Rock Mechanics and Rock Engineering (ISRM) (Muralha et al., 2014). Hence, we define W_f as 120 mm. From Table 3, w_c and f are 7.8 mm and 50 mm, respectively. According to Eq. (1), the OD is calculated to be 769 mm. Therefore, the recommended shooting distance for joint specimens with size of 100 mm × 100 mm × 100 mm is 800 mm.

In this experiment, the morphological change of the shear surface was observed from the side wall of the upper block of 3DP joint specimen (Fig. 9). Due to the influence of refraction, it is necessary to choose a suitable shooting angle r. Hence, we set the center of profile on side wall of the upper block as the origin O and take OD as the radius to rotate the CCD camera counterclockwise. The images of surface morphology at six angles (i.e. 20°, 30°, 40°, 50°, 60° and 70°) were taken and their areas (A_p) of joint surface were obtained by counting the number of red pixels in research area (Table 4). The results show that when the shooting angle is low, part of morphology of the joint surface is occluded by some morphology with high undulation, making its value of A_p is small. As the angle increases, the occluded morphology gradually appears and the

Table 3
Parameters of the CCD camera.

Property	Value	Unit
Maximum resolution	1920 × 1080	ppi × ppi
Maximum FPS @ Maximum Res	12300	fps
Sensor type	CMOS − Proprietary	
Sensor size	13.9 × 7.8	mm × mm
Sensor format	1	in
Distance to lens	50	mm

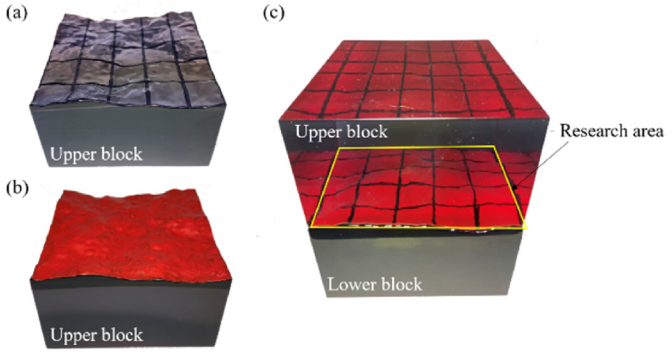

Fig. 7. Surface treatment of upper block of 3DP joint specimen: (a) Partition of joint surface, (b) coloring of joint surface, and (c) evaluation for surface treatment.

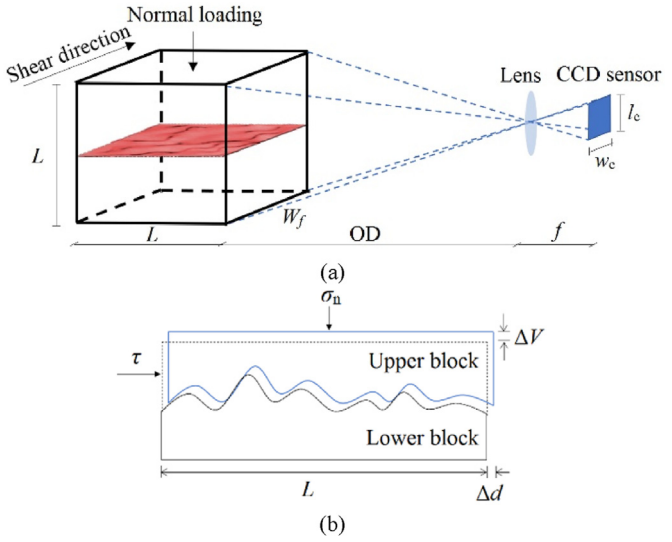

Fig. 8. Determination of object distance: Schematic diagrams of (a) CCD imaging and (b) shear process.

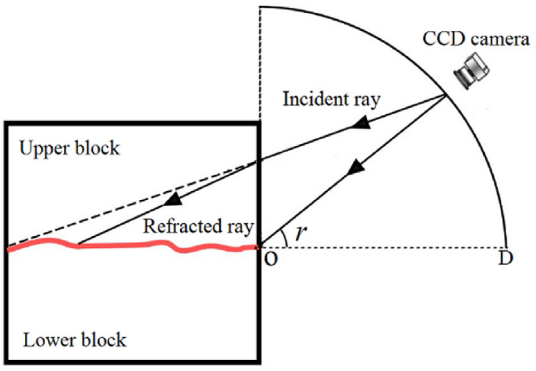

Fig. 9. Schematic diagram of the influence of refraction on imaging.

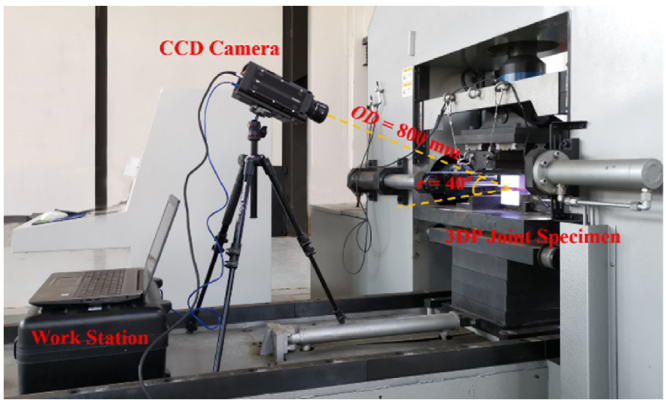

Fig. 10. Laboratory configuration of the CCD camera.

value of A_p increases. However, with further increase in angle, the profile of side wall becomes smaller causing the A_p decrease accordingly, and the observed joint surface is incomplete. When the shooting angle is 40°, the A_p reaches the maximum, which means that the joint morphology obtained at this angle is relatively rich and easy to observe the change. Consequently, the shooting angle is set to 40° in this study, as shown in Fig. 10.

3.2. Correction of the images recorded during shearing

To effectively observe the shear zone, it is necessary to correct the skew of the captured images as displayed in Fig. 11, and the specific steps are as follows:

Step 1: A rectangular coordinate system is set up with point *A* as the coordinate origin. The lengths of side *AB*, which can be used as reference side, in the captured image and the front view are the same because the shooting is performed with the midpoint of front side as the center of the image. Then, one-fifth of the length of this side is used as the standard length (l_{st}) of each small grid. This work is done in MATLAB with the image processing technique. Take one captured image as an example (Fig. 12a), the measured length of reference side is 450 pixels, and the l_{st} is one-fifth of the length of reference side, which is 90 pixels.

Step 2: Under perspective projection, each corresponding pixel is related by (Criminisi, 1999):

Table 4
Statistics of the surface morphology obtained from different shooting angles.

r (°)	Shooting image	A_p (10^4 pixel)	r (°)	Shooting image	A_p (10^4 pixel)
20		20.2	50		23.2
30		22.9	60		21.2
40	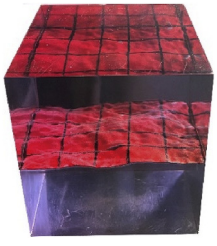	24.5	70		20.5

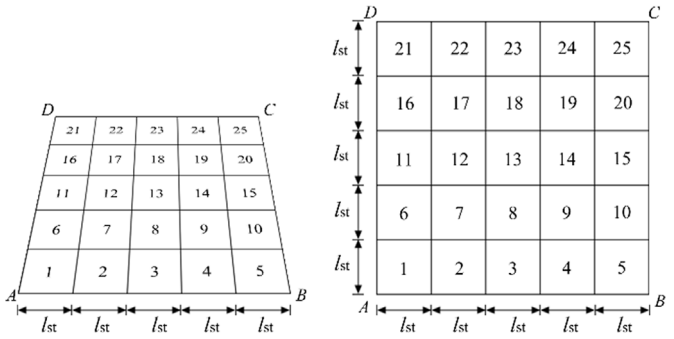

Fig. 11. Schematic diagram of image correction: Grids (a) before and (b) after correction.

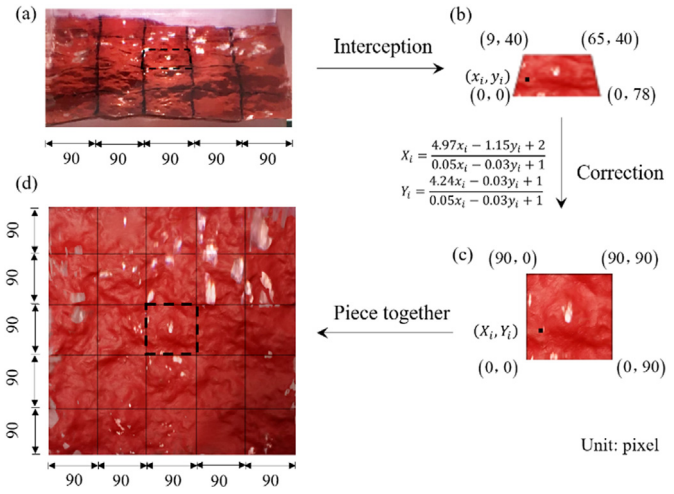

Fig. 12. Correction process of shear area: (a) Determining the standard length of each grid, (b) identification of grid's pixel coordinates, (c) grid correction, and (d) corrected joint morphology.

$$\left.\begin{aligned} X_i &= \frac{ax_i + by_i + c}{gx_i + hy_i + 1} \\ Y_i &= \frac{dx_i + ey_i + f}{gx_i + hy_i + 1} \end{aligned}\right\} \tag{2}$$

where (x_i, y_i) denote the pixel coordinates of the ith point on the captured image; (X_i, Y_i) denote the pixel coordinate corresponding to the ith point on the corrected image; and a, b, c, d, e, f, g and h are the projection variation coefficients. Taking one grid as the research object, the pixel coordinates of its four vertices are (x_1, y_1), (x_2, y_2), (x_3, y_3) and (x_4, y_4). Setting the pixel (x_1, y_1) as the calibration point before and after image correction, the pixel coordinates of these four vertices in the corrected image should be (x_1, y_1), $(x_1 + l_{st}, y_1)$, $(x_1, y_1 + l_{st})$ and $(x_1 + l_{st}, y_1 + l_{st})$, respectively. The above coordinate points are substituted into Eq. (2), and then the projection variation coefficients are determined. Taking the grid 13 as an example, it is first intercepted from captured image (Fig. 12b). The pixel coordinates of its four vertices are then identified in MATLAB as (0, 0), (0, 78), (9, 40) and (65, 40). For these four vertices on corrected image, their pixel coordinates are (0, 0), (90, 0), (0, 90) and (90, 90). Hence, the projection variation coefficients a, b, c, d, e, f, g and h could be obtained by solving Eq. (2), which are 4.97, −1.15, 2, 4.24, −0.03, 1, 0.05 and −0.03, respectively.

Step 3: According to the projection variation coefficients of the corresponding grid, all the pixel coordinates recorded in this grid are corrected with Eq. (2) to obtain the corrected image (Fig. 12c). Finally, all the grids of the joint surface are corrected and integrated according to the corresponding positioning (Fig. 12d).

3.3. Identification of damaged area

To evaluate shear failure, it is necessary to identify the damaged area from the corrected images. The damaged area is white due to the fading of the red pigment caused by the friction when upper block climbs or slides over the lower block (Fig. 13a). It was precisely because the color of the damaged area was different from that of the undamaged area, we used image segmentation in image processing to extract the contour of the damaged area, and then calculated its area. This work was done in the OpenCV (Xie et al., 2013; Sivkov et al., 2020). First, the color image was converted to an 8-bit grayscale image to reduce the interference of color in identifying the joint surface morphology (Fig. 13b). Then, the obtained grayscale image was binarized to highlight its outline (Fig. 13c). Finally, all the contours of the damaged area were extracted (Fig. 13d), and the total of their areas is the total sheared area. Consequently, the above method could be used to quantitatively determine the shear failure of the surface morphology of 3DP joint specimens under a certain shear displacement.

4. Experiments and validation

4.1. Direct shear test

A self-developed shear apparatus called MS-DST was used to conduct the direct shear test on the 3DP joint specimens (Huang et al., 2020). It consists of a loading system and a data acquisition system (Fig. 14a). In the shear chamber (Fig. 14b), the shear box is available to host cubic specimens with a side length of 100–400 mm,

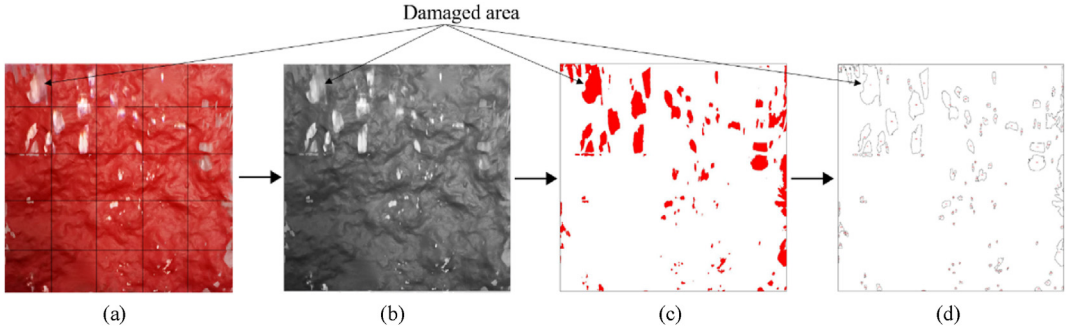

Fig. 13. Schematic diagram of image processing: (a) Color image, (b) gray image, (c) binary image, and (d) outline drawing.

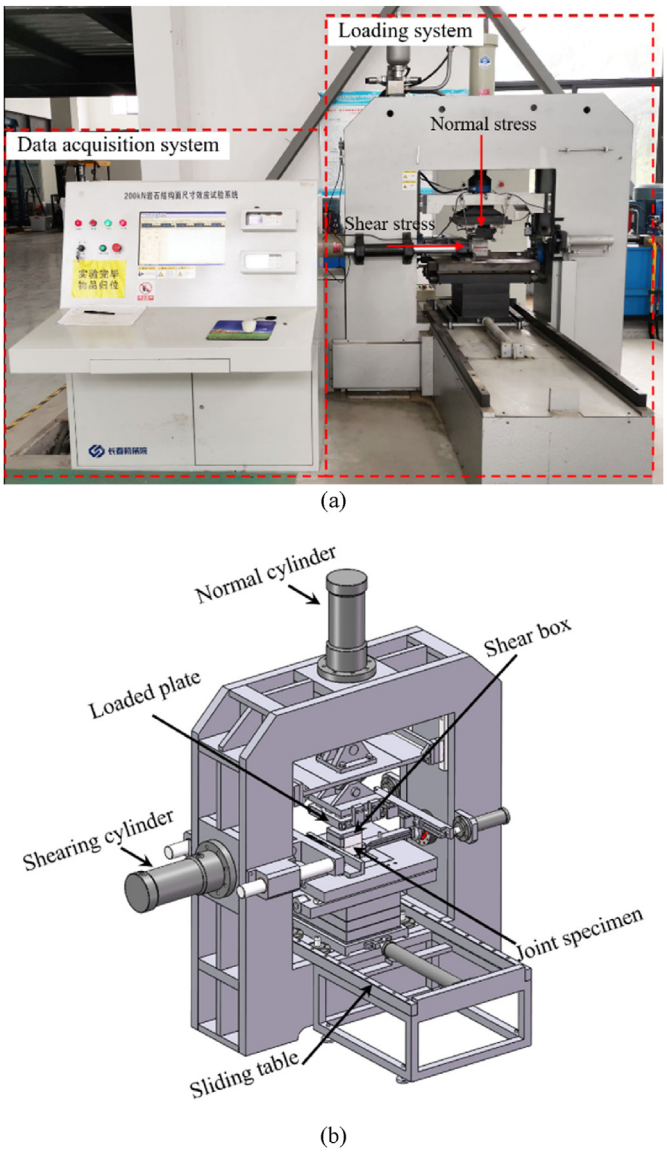

Fig. 14. Direct shear apparatus: (a) Shear system and (b) its shear chamber.

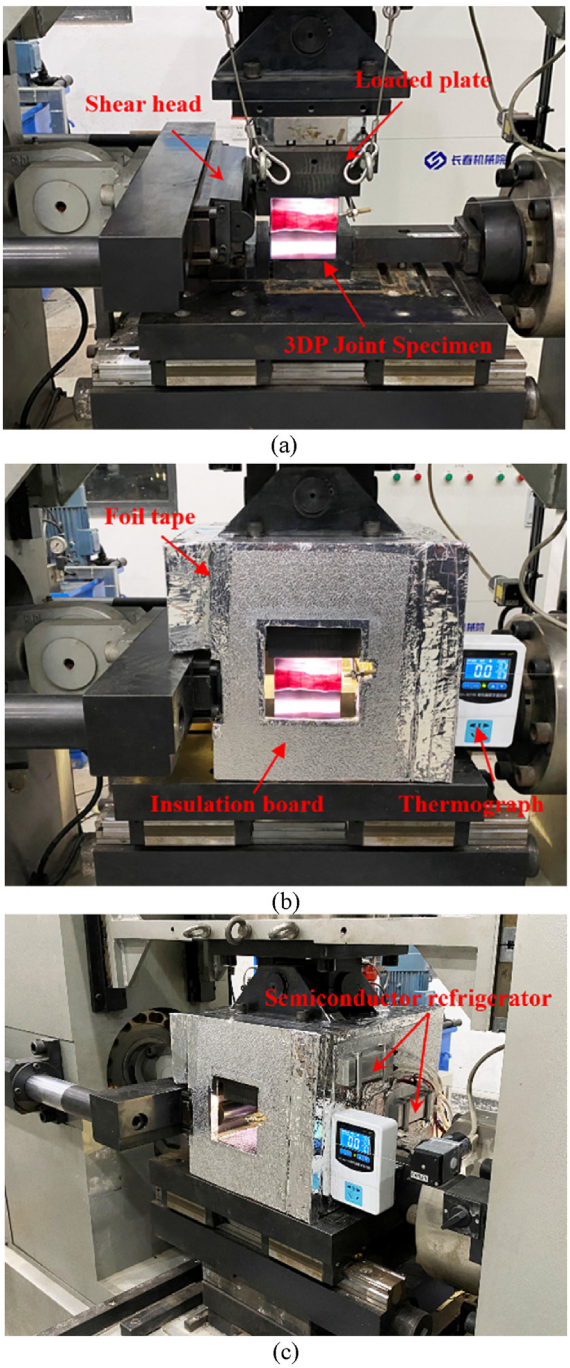

Fig. 15. Preparation before shearing: (a) Placement of the specimen, (b) front of the barrier, and (c) side of the barrier.

and the maximum shear displacement is 300 mm. The maximum loading capacities in both axial and horizontal directions are 200 kN, with a precision of 200 N. The axial load was applied to the specimen by a loaded plate, and the horizontal load was applied, with a given shear rate set by the user, by a servo-controlled loading ram connected to the upper part of the shear box. Horizontal and vertical displacements were measured externally in the shear chamber by two linear variable differential transformers (LVDTs) with a range of 50 mm and a precision of 12 μm.

Before the test, we first put the frozen specimen in the shear box and allowed the normal loaded plate and the shear head to respectively shift downward and forward until they contacted the shear box (Fig. 15a). To prevent the specimen from being exposed to laboratory temperature, we built a barrier around the specimen with some insulation boards, and sealed it with foil tapes. An observation port was reserved on the insulation board facing the CCD camera, which enable the CCD camera to shoot images of the joint surface (Fig. 15b). Two semiconductor refrigerators and a temperature sensor were placed in the barrier to ensure the temperature around the specimen to be 0 °C throughout the test (Fig. 15c). This barrier is designed according to the set-up of shear chamber and will not affect the operation of each shear system. At the beginning of the test, the normal stress (σ_n) increased to 0.5 MPa at a rate of 0.01 MPa/s. When the normal displacements stabilized under the applied normal load, the shear displacement was continuously invoked at a rate of 0.1 mm/min (Muralha et al., 2014). The test was terminated when the shear strength reached the residual value, and its entire shear process was recorded using the CCD camera at a frame rate of 20 frame/s.

According to the monitoring data of thermometer shown in Fig. 16a, the temperature variation of specimen does not exceed 5 °C. Judging from the test results in Section 2.2, it could be considered

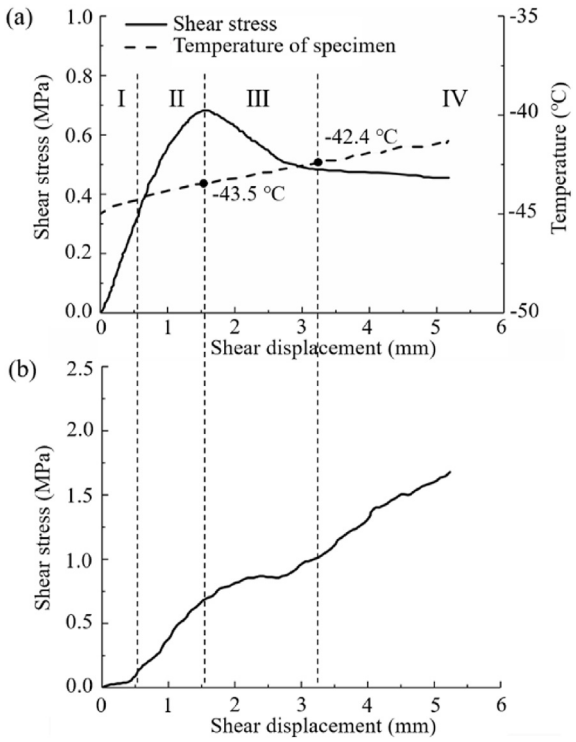

Fig. 16. Shear behaviors of 3DP specimen: (a) Shear stress and temperature versus shear displacement, and (b) shear stress versus shear displacement.

that the mechanical properties of specimen were similar to that of the natural rock during the shear process. However, due to the temperature of 3DP specimen was far below 0 °C, the water vapor in the air around the specimen condensed and formed frost covering its surface, making the captured image blurry. To this end, we gently wiped the surface with dry tissues every 5 s till the end of the test to ensure that the captured image was clear.

From the experimental results shown in Fig. 16, the shear behaviors of 3DP specimens were similar to that of natural joints. It indicated that this approach provides a possibility for analyzing the shear failure process of joints.

4.2. Mechanism of shear failure

The CCD camera recorded the image of joint surface at each shear displacement in Fig. 16, and we extracted four images represent shearing Stages I, II, III and IV from it. Furthermore, an image before shear test was also extracted for comparison, as shown in Fig. 17. Initially, upper block was placed over the fixed lower block without applied normal stress, and there was no damaged area on the joint surface (Fig. 17a). At the Stage I, the shear stress linearly increased with the shear displacement (Fig. 16a), and the upper block began to climb due to the domination of sliding friction over the sliding resistance, causing small dilation in the normal displacement (Fig. 16b). The damaged area appeared on the joint surface (white areas in the grids 17 and 18 of Fig. 17b. Note that the grid numbers refer to Fig. 11 due to the fading of the red pigment caused by sliding. At the Stage II, the shear stress nonlinearly increased with the further increase in shear displacement (Fig. 16a), and the dilation was heightened (Fig. 16b). The damaged area of the joint surface expanded (Fig. 17c), which can be seen from the increase in grids 5, 6, 16 and 21. From Stage I to Stage II, we can find that at the pre-peak stage, the shearing of upper and lower

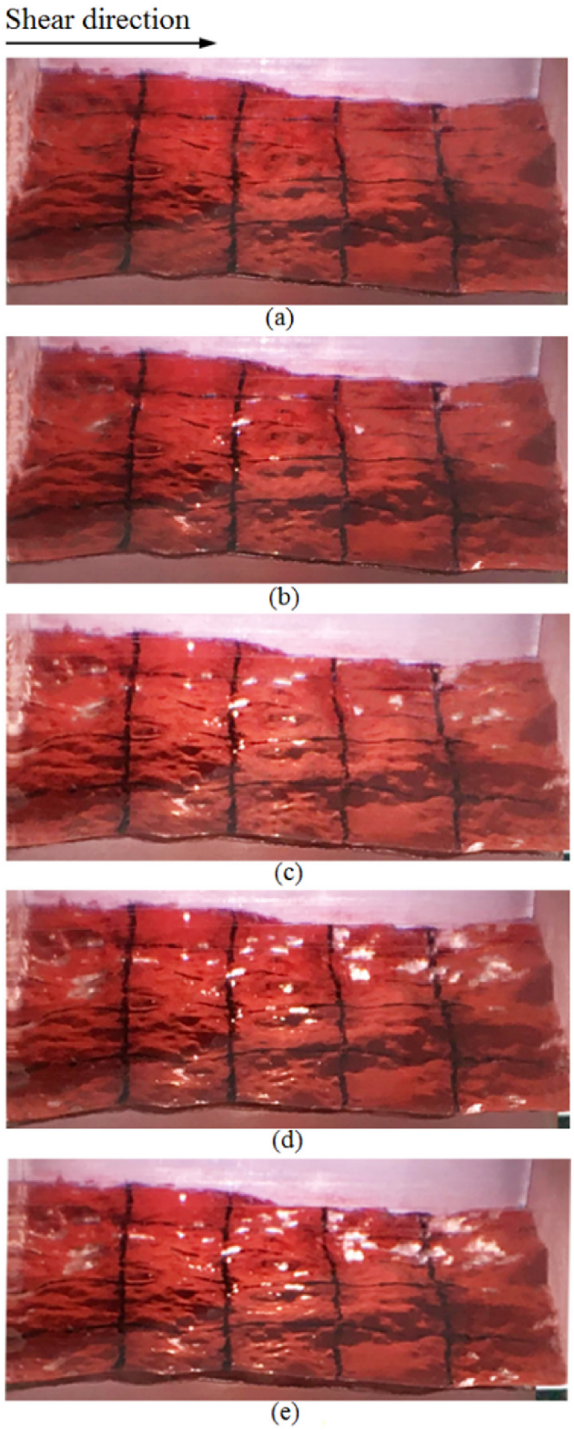

Fig. 17. Joint surface of 3DP specimen at (a) pre-shearing stage, (b) Stage I, (c) Stage II, (d) Stage III, and (e) Stage IV.

blocks underwent the wear of asperities in small shear displacement to the dilation of the undulation in large shear displacement.

At the post-peak stage (Stage III), the peak shear stress decreased with the shear displacement (Fig. 16a) because of the generation of new frictional contact surfaces (Huang et al., 2020). And more damaged area occurred (Fig. 17d) due to the further shearing through the shearing-off steeper asperities and contact of two blocks. With the increase of contact area of two blocks, the shear stress decreased to a point called residual shear strength (Fig. 16a), while the joint continued to dilation due to presence of

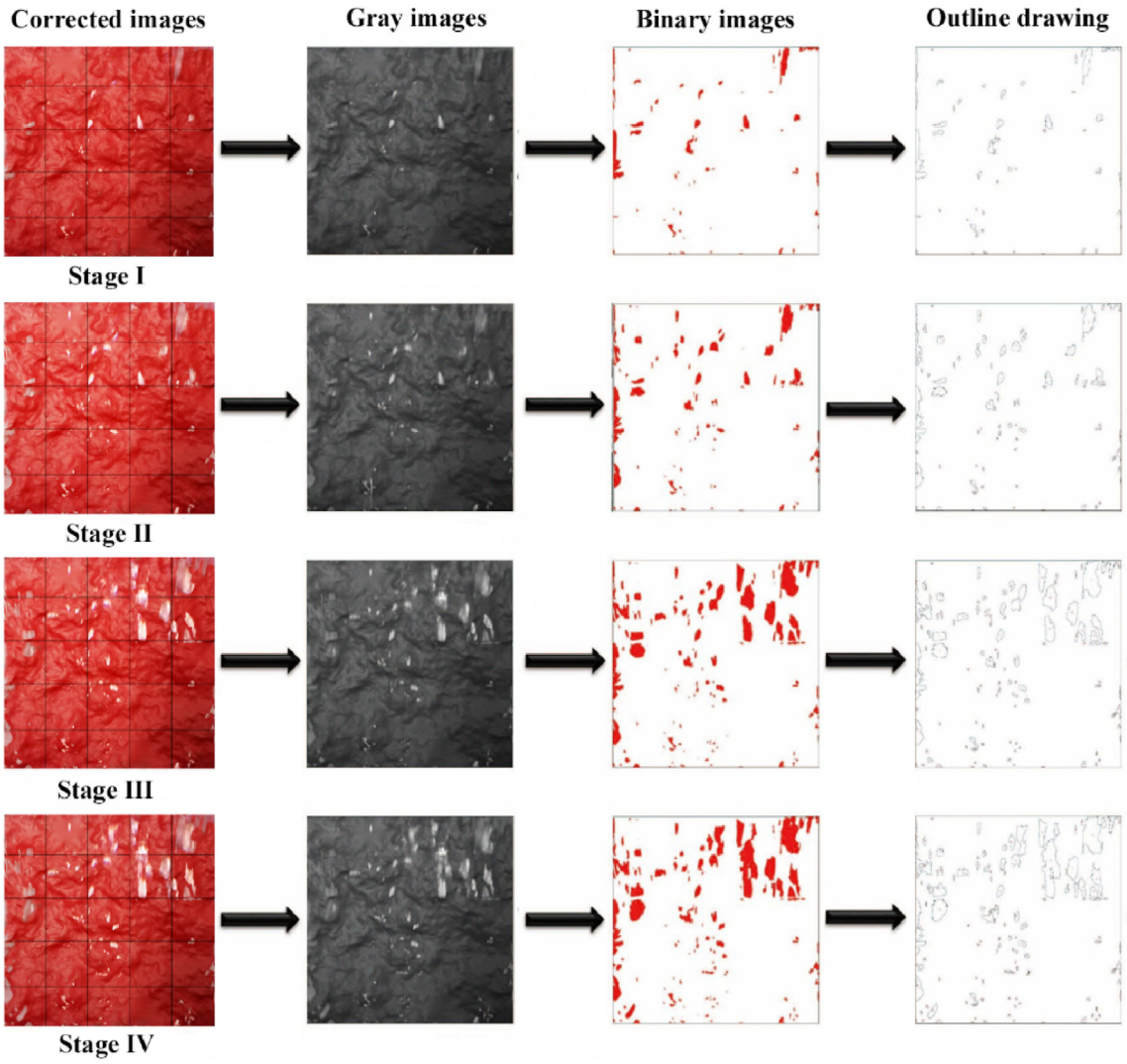

Fig. 18. Extraction of the damaged areas at different shear stages.

Table 5
Sheared areas under different displacements.

Stage No.	Shear displacement (mm)	Number of damaged areas	Total sheared area (mm^2)
I	0.5	51	247.35
II	1.6	82	441.49
III	2.6	108	851.81
IV	4.2	120	993.33

new steeper asperities (Fig. 16b). At the residual stage (Stage IV), all the steeper asperities were sheared-off during shearing and provided constant residual shear strength (Fig. 16a) and constant damaged area (Fig. 17e).

4.3. Description of total sheared area

According to the correction method proposed in Section 3, the four images representing stages I, II, III and IV were imported into the OpenCV to determine the damaged area of the joint surface and to qualitatively illustrate the changes in the rock joint during the shearing process. The result is shown in Fig. 18. Through calculating the total sheared area of four stages (Table 5), it is found that the accelerated expansion of shear failure is mainly concentrated at Stage III, i.e. the additional wear of the joint surface after the peak shear strength is more than that before the peak shear strength. The observations illustrate that the shear failure of rock joints at the stress softening stage is more severe, which should be considered in the construction of shear strength models.

5. Limitation

Although the developed method can realize the observation of the progressive failure of sheared joints, its limitations should be noted. First, the 3DP joint specimen is sensitive to temperature. The influence of the change in temperature on the shear properties of 3DP specimen is not considered. The 3DP joint specimen requires a low-temperature environment, which increases the complexity of direct shear test. It is necessary to find a material with strong suitability and low cost. Second, in order to capture the damage of the joint surface during shearing, the proposed method requires that at least one side of the shear box is not closed. However, the conventional shear box is basically made of a closed steel plate that cannot be seen through, which limits the applicability of the method. Some multifunctional shear apparatus should be further developed. Third, the outside surface of the sample will be fogged due to the

unavoidable temperature difference, resulting in blurry images taken by CCD camera. Although we alleviate this situation by manually wiping the fog, it cannot guarantee that all the images are clear. This brings difficulties to analyze the shear failure of the joints in real time. The low-temperature shearing technology should be further optimized. Fourth, the proposed correction method for shear image is only applied to the sheared joint without fractures, and the applicability should be further validated in the future.

Additionally, the 3DP sample only preliminarily proves the similarity to the rock-based joint from the basic mechanical property test and there is no comparison with specific rock joints, which should be further studied. Furthermore, this study initially investigates the changes in joint morphology under different shear displacements, and additional tests need to be conducted to gain its relation with the shear strength.

6. Conclusions

A systematic technique, including the preparation of 3DP joints, the shooting of shear process and the correction of shear image, is employed to realize a visualized shear test for rock joints. The capability of the proposed method to identify the damaged area on joint surface at each shear stage is validated. The following conclusions are drawn from this study:

(1) Visualized joints can be made with a type of transparent photopolymer resin called VeroClear 810, and a manufacturing operation using 3DLS and 3DP techniques was described in detail. The mechanical properties, such as the peak stress, stress–strain curve and failure mode, of 3DP joint specimen after low-temperature freezing treatment (particularly at −45 °C) exhibited good similarity to that of the actual rock specimens.

(2) A CCD camera was employed to record the damaged area of joint surface with the increase in shear displacement. According to the experimental environment, the shooting position (800 mm) and shooting angle (40°) between the CCD camera and the 3DP specimen were determined, and a method was proposed for correcting the image recorded from the CCD camera. Besides, a barrier was designed according to the set-up of shear chamber to provide a low-temperature environment for the 3DP sample during shear process.

(3) From the shear results, the 3DP specimen exhibited similar shear behaviors to that of the actual rock. The damaged areas of joint surface in the four shear stages were identified, and it was found that the accelerated expansion of shear failure mainly occurred at the Stage III, which means that the additional wear of the joint surface after the peak shear strength was more than that before the peak shear strength.

Declaration of competing interest

The authors declare that they have no known competing financial interests or personal relationships that could have appeared to influence the work reported in this paper.

Acknowledgments

This experimental study was partially funded by the National Natural Science Foundation of China (Grant Nos. 41572299and 41831290), and the 3D-printed modeling work was supported by the Zhejiang Provincial Natural Science Foundation of China (Grant No. LY18D020003), which is gratefully acknowledged.

References

Asadizadeh, M., Moosavi, M., Hossaini, M.F., 2017. Shear strength and cracking process of non-persistent jointed rocks: an extensive experimental investigation. Rock Mech. Rock Eng. 51 (2), 415–428.
Babanouri, N., Karimi, N.S., 2015. Modeling spatial structure of rock fracture surfaces before and after shear test: a method for estimating morphology of damaged zones. Rock Mech. Rock Eng. 48 (3), 1051–1065.
Barton, N., 1973. Review of a new shear-strength criterion for rock joints. Eng. Geol. 7 (4), 287–332.
Barton, N., 1977. The shear strength of rock joints in theory and practice. Rock Mech. 10 (1–2), 1–54.
Barton, N., 2013. Shear strength criteria for rock, rock joints, rockfill and rock masses: problems and some solutions. J. Rock Mech. Geotech. Eng. 5 (4), 249–261.
Chen, Z.W., Li, Z.Y., Li, J.J., 2019. 3D printing of ceramics: a review. J. Eur. Ceram. Soc. 39 (4), 661–687.
Criminisi, A., Reid, I., Zisserman, A., 1999. A plane measuring device. Image Vis Comput. 17 (8), 625–634.
Fan, X., Lin, H., Lai, H.P., 2019. Numerical analysis of the compressive and shear failure behavior of rock containing multi-intermittent joints. Compt. Rendus Mec. 347 (1), 33–48.
Fereshtenejad, S., Song, J.J., 2016. Fundamental study on applicability of powder-based 3D printer for physical modeling in rock Mechanics. Rock Mech. Rock Eng. 49 (6), 2065–2074.
Ge, Y., Tang, H., Eldin, M., 2016. Evolution process of natural rock joint roughness during direct shear tests. Int. J. GeoMech. E4016013, 1–10.
Grasselli, G., 2001. Shear Strength of Rock Joints Based on Quantified Surface Description. PhD Thesis. École Polytechnique Fédérale de Lausanne, Switzerland.
Grasselli, G., Wirth, J., Egger, P., 2002. Quantitative three-dimensional description of a rough surface and parameter evolution with shearing. Int. J. Rock Mech. Min. Sci. 39 (6), 789–800.
Grasselli, G., Egger, P., 2003. Constitutive law for the shear strength of rock joints based on three-dimensional surface parameters. Int. J. Rock Mech. Min. Sci. 40 (1), 25–40.
Grasselli, G., 2006. Manuel rocha medal recipient shear strength of rock joints based on quantified surface description. Rock Mech. Rock Eng. 39 (4), 295–314.
Hedayat, A., Pyrak, L.J., Bobet, A., 2014. Precursors to the shear failure of rock discontinuities. Geophys. Res. Lett. 41 (15), 5467–5475.
Huang, M., Du, S.G., Luo, Z.Y., 2013. Study of inverse controlling technology for series scales similar surface model making of rock joint. Rock Soil Mech. 34 (4), 1211–1216 (in Chinese).
Huang, M., Hong, C., Du, S., et al., 2020. Experimental technology for the shear strength of the series-scale rock joint model. Rock Mech. Rock Eng. 53, 5677–5695.
Ishida, T., Kanagawa, T., Kanaori, Y., 2010. Source distribution of acoustic emissions during an in-situ direct shear test: implications for an analog model of seismogenic faulting in an inhomogeneous rock mass. Eng. Geol. 110 (3–4), 66–76.
Jaber, J., Conin, M., Deck, O., et al., 2020. Investigation of the mechanical behavior of 3D printed polyamide-12 joints for reduced scale models of rock mass. Rock Mech. Rock Eng. 53, 2687–2705.
Jafari, M.K., Pellet, F., Boulon, M., 2004. Experimental study of mechanical behaviour of rock joints under cyclic loading. Rock Mech. Rock Eng. 37 (1), 3–23.
Jiang, C., Zhao, G.F., 2015. A preliminary study of 3D printing on rock Mechanics. Rock Mech. Rock Eng. 48 (3), 1041–1050.
Jiang, Q., Feng, X.T., Gong, Y.H., 2016a. Reverse modelling of natural rock joints using 3D scanning and 3D printing. Comput. Geotech. 73, 210–220.
Jiang, C., Zhao, G.F., Zhu, J., 2016b. Investigation of dynamic crack coalescence using a gypsum-like 3D printing. Material. Rock Mech. Rock Eng. 49 (10), 3983–3998.
Jing, L., Stephansson, O., Nordlund, E., 1993. Study of rock joints under cyclic loading conditions. Rock Mech. Rock Eng. 26 (3), 215–232.
Johnston, I.W., Lam, T., 1989. Shear behavior of regular triangular concrete/rock joints-analysis. Geotech. Eng. 115 (5), 711–727.
Ju, Y., Xie, H., Zheng, Z., 2014. Visualization of the complex structure and stress field inside rock by means of 3D printing technology. Chin. Sci. Bull. 59 (32), 3109–3119.
Ju, Y., Wang, L., Ma, G., 2017. Visualization and transparentization of the structure and stress field of aggregated geomaterials through 3D printing and photoelastic techniques. Rock Mech. Rock Eng. 50 (6), 1383–1407.
Ju, Y., Xie, H., Zhao, X., 2018. Visualization method for stress-field evolution during rapid crack propagation using 3D printing and photoelastic testing techniques. Sci. Rep. 8 (1), 4353.
Kong, L., Ostadhassan, M., Li, C., 2018. Can 3-D printed gypsum samples replicate natural rocks? An experimental study. Rock Mech. Rock Eng. 51 (10), 3061–3074.
Koyama, T., Li, B., Jiang, Y., 2008. Coupled shear-flow tests for rock fractures with visualization of the fluid flow and their numerical simulations. Int. J. GeoMech. 2 (3), 215–227.
Kulatilake, P.H.S.W., Shou, 1995. New peak shear strength criteria for anisotropic rock joints. Int. J. Rock Mech. Min. Sci. Geomech. Abstr. 32 (7), 673–697.
Kumar, R., Verma, A.K., 2016. Anisotropic shear behavior of rock joint replicas. Int. J. Rock Mech. Min. Sci. 90, 62–73.

Kuo, H.J., Huang, C.Y., Wang, W.H., et al., 2017. The study on surface characteristics of high transmission components by 3D printing technique. In: Proceedings of the International Conference on Optical and Photonics Engineering, pp. 1–6. Singapore.
Lee, H.S., Park, Y.J., Cho, T.F., 2001. Influence of asperity degradation on the mechanical behavior of rough joints under cyclic shear loading. Int. J. Rock Mech. Min. Sci. 38 (7), 967–980.
Li, B., Jiang, Y.J., Mizokami, T., 2014. Anisotropic shear behavior of closely jointed rock masses. Int. J. Rock Mech. Min. Sci. 71, 258–271.
Liu, P., Ju, Y., Ranjith, P.G., 2016. Visual representation and characterization of three-dimensional hydrofracturing cracks within heterogeneous rock through 3D printing and transparent models. Int. J. Cloth. Sci. Technol. 3 (3), 284–294.
Liu, P., Gervasoni, S., Madonna, C., et al., 2020. Response of remanent magnetization to deformation in geological processes using 3D-printed structures. Earth Planet Sci. Lett. 539, 116241.
Muralha, J., Grasselli, G., Tatone, B., et al., 2014. ISRM suggested method for laboratory determination of the shear strength of rock joints: revised version. Rock Mech. Rock Eng. 47 (1), 291–302.
Özgür, S., Bahtiyar, Ü., 2015. Assessment of tunnel portal stability at jointed rock mass: a comparative case study. Comput. Geotech. 64, 72–82.
Park, J.W., Song, J.J., 2013. Numerical method for the determination of contact areas of a rock joint under normal and shear loads. Int. J. Rock Mech. Min. Sci. 58, 8–22.
Peng, L., Yang, J., Feng, G., 2018. CT identification and fractal characterization of 3D propagation and distribution of hydrofracturing cracks in low–permeability heterogeneous rocks. J. Geophys. Res. Solid Earth 123 (3), 2156–2173.
Pua, L.M., Caicedo, B., Castillo, D., Caro, S., 2018. Development of a 3D clay printer for the preparation of heterogeneous models. In: Proceedings of the 9th International Conference on Physical Modelling in Geotechnics, pp. 155–160.
Roosta, R.M., Sadaghiani, M.H., Pak, A., 2006. Rock joint modeling using a visco-plastic multilaminate model at constant normal load condition. Geotech. Geol. Eng. 24 (5), 1449–1468.
Saeb, S., Amadei, B., 1992. Modelling rock joints under shear and normal loading. Int. J. Rock Mech. Min. Sci. 29 (3), 267–278.
Singh, M., Rao, K.S., Ramamurthy, T., 2002. Strength and deformational behaviour of a jointed rock mass. Rock Mech. Rock Eng. 35 (1), 45–64.
Sivkov, S., Novikov, L., Romanova, G., et al., 2020. The algorithm development for operation of a computer vision system via the OpenCV library. Procedia Comput. Sci. 169, 662–667.
Tan, Z.H., Tang, C.A., Zhu, W.C., 2007. Infrared thermal image study on failure of granite with hole. Key Eng. Mater. 353–358, 2313–2316.
Tang, H.M., Ge, Y.F., Wang, L.Q., 2012. Study on estimation method of rock mass discontinuity shear strength based on three-dimensional laser scanning and image technique. J. Earth Sci. 23 (6), 908–913.
Tohsing, K., Schrempf, M., Riechelmann, S., et al., 2013. Measuring high-resolution sky luminance distributions with a CCD camera. Appl. Opt. 52 (8), 1564–1573.
Wang, L., Ju, Y., Xie, H., et al., 2017. The mechanical and photoelastic properties of 3D printable stress-visualized materials. Sci. Rep. 7, 10918.
Wong, L., Einstein, H.H., 2009. Crack coalescence in molded gypsum and carrara marble: Part 1. Macroscopic observations and interpretation. Rock Mech. Rock Eng. 42 (3), 475–511.
Wu, Y., Mcgarry, F.J., Zhu, B., 2005. Temperature effect on mechanical properties of toughened silicone resins. Polym. Eng. Sci. 45 (11), 1522–1531.
Wu, F., Liu, J., Liu, T., et al., 2009. A method for assessment of excavation damaged zone (EDZ) of a rock mass and its application to a dam foundation case. Eng. Geol. 104 (3), 254–262.
Xia, C.C., Tang, Z.C., Xiao, W.M., 2014. New peak shear strength criterion of rock joints based on quantified surface description. Rock Mech. Rock Eng. 47 (2), 387–400.
Xia, Y., Zhang, C., Zhou, H., et al., 2020. Mechanical behavior of structurally reconstructed irregular columnar jointed rock mass using 3D printing. Eng. Geol. 268, 105509.
Xie, G., Lu, W., 2013. Image edge detection based on opencv. Int. J. Electron. 1 (2), 104–106.
Zhang, G., Karakus, M., Tang, H., 2014. A new method estimating the 2D Joint Roughness Coefficient for discontinuity surfaces in rock masses. Int. J. Rock Mech. Min. Sci. 72, 191–198.
Zhang, X., Jiang, Q., Na, C., 2016. Laboratory investigation on shear behavior of rock joints and a new peak shear strength criterion. Rock Mech. Rock Eng. 49 (9), 1–18.
Zhao, X.G., Wang, J., Cai, M., et al., 2014. Influence of unloading rate on the strainburst characteristics of beishan granite under true-triaxial unloading conditions. Rock Mech. Rock Eng. 47 (2), 467–483.
Zhou, T., Zhu, J.B., 2018. Identification of a suitable 3D printing material for mimicking brittle and hard rocks and its brittleness enhancements. Rock Mech. Rock Eng. 51 (3), 765–777.
Zhou, T., Zhu, J.B., Ju, Y., Xie, H.P., 2019. Volumetric fracturing behavior of 3D printed artificial rocks containing single and double 3D internal flaws under static uniaxial compression. Eng. Fract. Mech. 205, 190–204.

Dr. Man Huang is presently working as a professor in Shaoxing University, Zhejiang Province, China. He obtained his PhD from Tongji University, China. His research focuses on the mechanical characteristics of rock joint including joint surface roughness and size effect of shear strength. He has chaired and participated in a number of National Natural Science Foundation and published more than 60 papers in the domestic and international journals. He was granted the Second Prize of National Technology Invention, the First Prize of Zhejiang Technology Invention and the First Prize of Zhejiang Technology Progress Award. He is a member of International Society for Rock Mechanics and Rock engineering (ISRM) and Chinese Society for Rock Mechanics and Engineering (CSRME).